View metadata, citation and similar papers at core.ac.uk

brought to you by CORE

provided by Missouri University of Science and Technology (Missouri S&T): Scholars' Mine

Missouri University of Science and Technology

Scholars' Mine

Mechanical and Aerospace Engineering Faculty Research & Creative Works

Mechanical and Aerospace Engineering

01 Apr 2018

Additive Manufacturing of Transparent Fused Quartz

Junjie Luo

John M. Hostetler

Luke Gilbert

Jonathan T. Goldstein

et. al. For a complete list of authors, see https://scholarsmine.mst.edu/mec_aereng_facwork/4057

Follow this and additional works at: https://scholarsmine.mst.edu/mec_aereng_facwork

 Part of the Mechanical Engineering Commons

Recommended Citation

J. Luo et al., "Additive Manufacturing of Transparent Fused Quartz," *Optical Engineering*, vol. 57, no. 4, SPIE, Apr 2018.

The definitive version is available at https://doi.org/10.1117/1.OE.57.4.041408

This Article - Journal is brought to you for free and open access by Scholars' Mine. It has been accepted for inclusion in Mechanical and Aerospace Engineering Faculty Research & Creative Works by an authorized administrator of Scholars' Mine. This work is protected by U. S. Copyright Law. Unauthorized use including reproduction for redistribution requires the permission of the copyright holder. For more information, please contact scholarsmine@mst.edu.

Optical Engineering

OpticalEngineering.SPIEDigitalLibrary.org

Additive manufacturing of transparent fused quartz

Junjie Luo
John M. Hostetler
Luke Gilbert
Jonathan T. Goldstein
Augustine M. Urbas
Douglas A. Bristow
Robert G. Landers
Edward C. Kinzel

SPIE.

Junjie Luo, John M. Hostetler, Luke Gilbert, Jonathan T. Goldstein, Augustine M. Urbas, Douglas A. Bristow, Robert G. Landers, Edward C. Kinzel, "Additive manufacturing of transparent fused quartz," *Opt. Eng.* **57**(4), 041408 (2018), doi: 10.1117/1.OE.57.4.041408.

Downloaded From: https://www.spiedigitallibrary.org/journals/Optical-Engineering on 12/17/2018
Terms of Use: https://www.spiedigitallibrary.org/terms-of-use

Additive manufacturing of transparent fused quartz

Junjie Luo,[a] John M. Hostetler,[a] Luke Gilbert,[a] Jonathan T. Goldstein,[b] Augustine M. Urbas,[b] Douglas A. Bristow,[a] Robert G. Landers,[a] and Edward C. Kinzel[a,*]
[a]Missouri University of Science and Technology, Mechanical and Aerospace Engineering, Rolla, Missouri, United States
[b]Air Force Research Laboratory, Materials and Manufacturing Directorate, Wright-Patterson Air-Force Base, Ohio, United States

Abstract. This paper investigates a filament-fed process for additive manufacturing (AM) of fused quartz. Glasses such as fused quartz have significant scientific and engineering applications, which include optics, communications, electronics, and hermetic seals. AM has several attractive benefits such as increased design freedom, faster prototyping, and lower processing costs for small production volumes. However, current research into glass AM has focused primarily on nonoptical applications. Fused quartz is studied here because of its desirability for use in high-quality optics due to its high transmissivity and thermal stability. Fused quartz filaments are fed into a CO_2 laser-generated molten region, smoothly depositing material onto the workpiece. Spectroscopy and pyrometry are used to measure the thermal radiation incandescently emitted from the molten region. The effects of the laser power and scan speed are determined by measuring the morphology of single tracks. Thin walls are printed to study the effects of layer-to-layer height. This information is used to deposit solid pieces including a cylindrical-convex shape capable of focusing visible light. The transmittance and index homogeneity of the printed fused quartz are measured. These results show that the filament-fed process has the potential to print transmissive optics. *© 2018 Society of Photo-Optical Instrumentation Engineers (SPIE)* [DOI: 10.1117/1.OE.57.4.041408]

Keywords: additive manufacturing; fused quartz; laser processing.

Paper 171586SSP received Oct. 6, 2017; accepted for publication Feb. 9, 2018; published online Mar. 6, 2018.

1 Introduction

Additive manufacturing (AM) has demonstrated significant promise in printing complex and unique three-dimensional (3-D) parts quickly and inexpensively. Although AM has been used for creating structural parts since the late 1980's,[1] printing refractive optics is still in its nascency. AM studies on printing optical transparent polymers include the 3-D printing,[2–4] inkjet printing,[5,6] selective laser sintering (SLS) followed by infiltration with index matched plastic,[7] and multiphoton stereolithography.[8] These processes are capable of printing low-power polymer optics, but lack the ability to be implemented with glasses and other inorganic materials that are required for higher-quality optics. Compared to polymers, glasses have greater transmissivity (particularly in the ultraviolet and infrared), lower coefficients of thermal expansion, and more temperature-stable indices of refraction.[9]

Conventional AM techniques such as selective laser melting/sintering (SLM/SLS), extrusion techniques, and binder jetting processes have been demonstrated for printing nontransparent glasses and ceramics.[10–15] Bubble entrapment, leading to optical scattering, limits the transparency. Entrapment is due to the high viscosity and surface tension of molten glass, which prevents bubbles from escaping due to buoyancy over the limited heating duration. Although Khmyrov et al.[14] demonstrated that this may be mitigated for properly sized quartz particles by depositing single layers using SLM. Two recent studies demonstrated that careful burnout of organic precursors and slow-high temperature densification can produce transparent silica structures using an extrusion[15] or stereolithography processes.[16] Another approach is to smoothly deposit parts from fully dense feedstock. This is similar to flame-working and has been previously used to figure micro-optics using a CO_2 laser by Veiko et al.[17,18] We previously demonstrated printing soda-lime glass parts using a filament-fed laser-heated process.[19] Similarly, Klein et al.[20] deposited single track wide, 3-D structures by allowing molten soda-lime glass to be drip through an orifice onto a computer-controlled stage. While soda-lime glass has a relatively low working temperature, fused quartz's working temperature (~1600°C) exacerbates the challenge of direct deposition.[9]

This paper presents a study of a laser-heated, filament-fed process for printing fused quartz. The influence of different parameters on the morphology of printed single tracks is explored, after which the optimum parameters are then used to print thin walls and cylinders to study the effect of layer height on the deposited morphology. The optimum layer height identified is then used to print a fully dense cube. This is followed by the deposition and testing of simple cylindrical lenses to demonstrate the potential for controlling the surface figure. Incandescent thermal radiation emitted by the molten glass during printing is observed spectroscopically and correlated with a basic thermal model for the process. Finally, the optical quality of the 3-D cube is demonstrated by measuring the transmittance and modulation transfer function (MTF).

2 Experimental Procedure

Figure 1 shows the experimental AM setup. A 125-W CW CO_2 laser (Synrad Evolution 125, $\lambda_0 = 10.6\ \mu m$) is focused on the intersection of the filament and the substrate. The CO_2 laser couples to a phonon mode in the fused quartz.[21] A 1-mm-thick fused quartz slide is used as the substrate and is fixed to a numerically controlled three-axis stage. The x and y stages (Thorlabs DDMS100) are driven by direct-drive brushless servomotors while a pantograph type

*Address all correspondence to: Edward C. Kinzel, E-mail: kinzele@mst.edu

0091-3286/2018/$25.00 © 2018 SPIE

Downloaded From: https://www.spiedigitallibrary.org/journals/Optical-Engineering on 12/17/2018
Terms of Use: https://www.spiedigitallibrary.org/terms-of-use

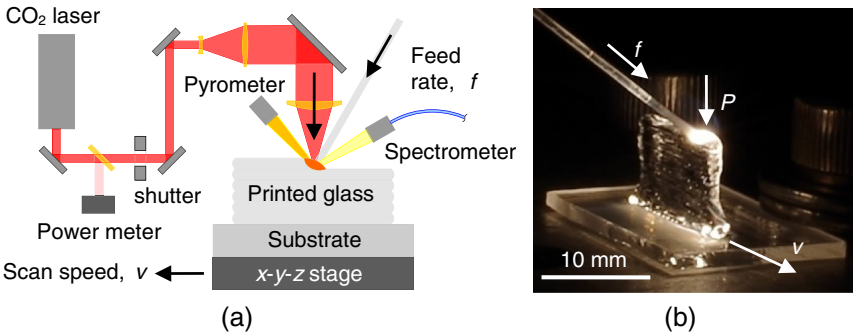

Fig. 1 (a) Illustration and (b) photograph of filament-fed fused quartz AM process.

lab-jack (Thorlabs L490MZ) is used to raise and lower the platform.

Previous work using soda-lime glass required preheating the substrate.[19] This proved not to be necessary for small pieces made of fused quartz, because the coefficient of thermal expansion is less than 10% that of soda-lime glass.[9] For larger pieces, heating of the substrate may be necessary due to larger thermal stresses. The filaments used in this work are GE 214 fused quartz rods with a nominal diameter of 0.5 mm. The full-width half-maximum (FWHM) diameter of the laser beam at this intersection is measured to be 300 μm using an Ophir NanoScan 2. A beam splitter is used to reflect 1% of the laser beam into a thermopile power meter (Ophir 10A –V1). By scaling this measured value, the power of the laser delivered to the molten region is obtained. For each experiment, the laser power is controlled at a constant level (producing a measured power variation of $\pm 1.5\%$). An OceanOptics USB-4000 fiber-coupled spectrometer (calibrated with an OceanOptics LS-1-CA 2800 K light source) is used with a 5-cm focal length lens to collect visible/NIR radiation emitted from the 1.5-mm-diameter interrogation region, centered on the laser-heated region.

For the following experiments, single tracks with a uniform height and width are created by a continuous feeding and laser melting of the filament. 3-D structures (thin walls and cubes) are then printed by repeating this process by lowering and offsetting the platform by set amounts varying between 0.126 and 0.294 mm.

3 Results and Discussion

3.1 *Single Track Results*

The properties of a printed part depend largely on the properties of constituent single tracks. To characterize the effects of the process parameters on the morphology of deposited parts, single tracks were printed over a range of parametric

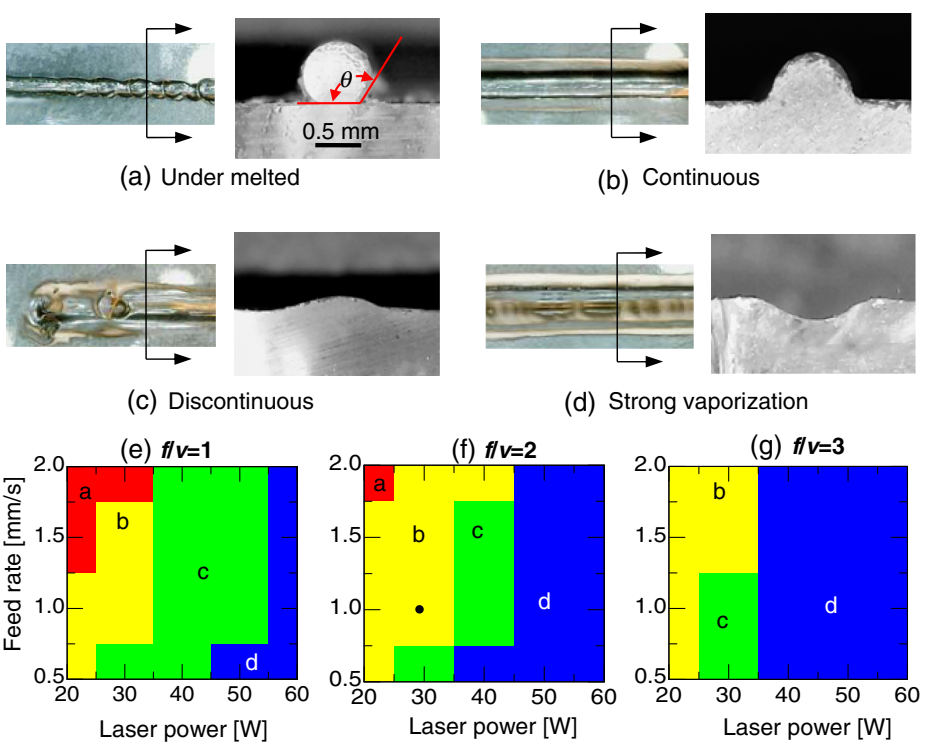

Fig. 2 (a–d) Top and cross-sectional photographs of the four morphological regimes for printed quartz tracks, and map of the morphological regimes with respect to laser power and filament feed rate for (e) $f/v = 1$, (f) $f/v = 2$, and (g) $f/v = 3$.

Downloaded From: https://www.spiedigitallibrary.org/journals/Optical-Engineering on 12/17/2018
Terms of Use: https://www.spiedigitallibrary.org/terms-of-use

combinations. For these tests, powers between 20 and 60 W (measured after the final lens) were used. Lower powers can be used with slower scan speeds or smaller filaments, but this results in lower volumetric deposition rates. Four general regimes were observed: (a) under melted, (b) continuous track, (c) discontinuous track, and (d) strong vaporization. Figures 2(a)–2(d) show photographs of each regime. These regimes are mapped as a function of the laser power incident on the melt pool and the filament feed rate in Figs. 2(e)–2(g) for three different feed rate to scan speed ratios, f/v.

An under melted track occurs when the absorbed energy is insufficient to fully melt the filament. The unmelted filament is deflected by the rigid substrate and eventually breaks. In order to achieve a continuous deposition, the laser must supply sufficient energy to fully melt the filament. We use the contact angle, θ, shown if Fig. 2(a), to distinguish the under melted ($\theta > 90$ deg) from the continuous regimes ($\theta \leq 90$ deg) based on when the contact angle, θ, of the track [shown if Fig. 2(a)]. As the laser energy increases beyond this threshold, surface tension causes the fused quartz to ball up at the end of the filament. The filament only makes contact with the substrate intermittently as it is advanced toward the intersection of the substrate and laser beam. In this state, vaporization of the filament also becomes evident. When the laser power is increased further, the rate of vaporization increases to a point where the rate of deposition of the fused quartz onto the substrate becomes negative, and material is removed to etch a groove into the substrate.

Figure 3 shows the measured cross-sectional area, A_c, of tracks printed with $f/v = 2$. The dashed line represents the cross-sectional area obtained from the conservation of mass between the fed filament and the printed track. The negative values of A_c correspond to vaporization of the substrate. The results show that the amount of vaporized mass increases with laser power and decreases with increasing feed rate.

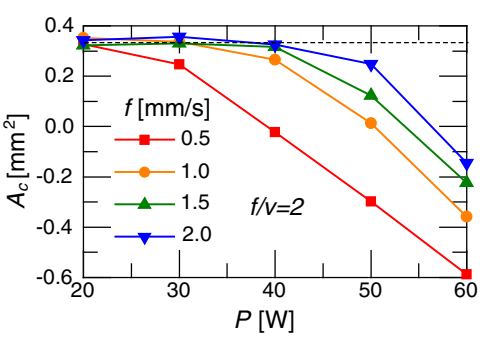

Fig. 3 Cross-section areas of all tracks made with $f/v = 2$.

3.2 *Single Track Wide Walls*

Thin walls were printed by depositing a track and subsequently lowering the substrate by a predefined height for consecutive track depositions. In these experiments, the substrate is scanned back and forth so that glass is continuously deposited. Correct selection of the layer height proves to be critical to successful wall deposition. If the layer height does not appropriately correspond to other deposition parameters, the wall will fail to be built due to a misalignment among the work piece, tip of the filament, and the laser beam.

Based on the results of the single track experiments, the parameters of $f = 1$ mm/s, $v = 0.5$ mm/s, and $P = 30$ W were selected for printing thin walls. These parameters produced a track with a height of $h_0 = 0.21$ mm. To identify the range of layer heights resulting in continuous walls, experiments were conducted with layer heights (changes in the height of the substrate between tracks) between 0.13 and 0.29 mm ($0.6\,h_0$ to $1.4\,h_0$). These experiments showed that continuous walls are deposited when the layer height is 0.17 to 0.21 mm ($0.8\,h_0$ to $1.0\,h_0$). Figure 4 shows representative samples of the thin wall morphologies.

When the layer height is too small, the intersection of the laser beam and filament tip is beneath the top of the previous layer. This results in the filament tip being deflected from the center of the molten region, preventing it from being fully melted. As shown in Fig. 4(a), the filament then pushes the printed wall with a force sufficient to distort the previously deposited layer, after which the filament is broken off at the feeder. When the layer height is appropriately set in accordance with the other process parameters, the filament may be fed into the molten region at each layer so that the printed wall is continuous. An example of a continuous wall is shown in Fig. 4(b). If the layer height exceeds the appropriate range, molten glass will begin to ball up at the tip of the filament. The diameter of the ball increases during the feeding process, and it will touch the previous layer intermittently as it gains mass and subsequently deposits it by contacting the substrate. This produces a two-dimensional (2-D) discontinuous wall shown in Fig. 4(c).

3.3 *Deposition of Solid 3-D Shapes*

The single wall-printing process requires the deposition of consecutive tracks in the vertical direction only. However, the printing of 3-D parts requires deposition in the horizontal direction as well. The addition of a third print dimension generates new challenges. Glass has a different refractive index than air, so any voids inside the 3-D part will scatter light. To further explore the potential for printing fused quartz, a $6 \times 6 \times 6$ mm cube was printed with the same

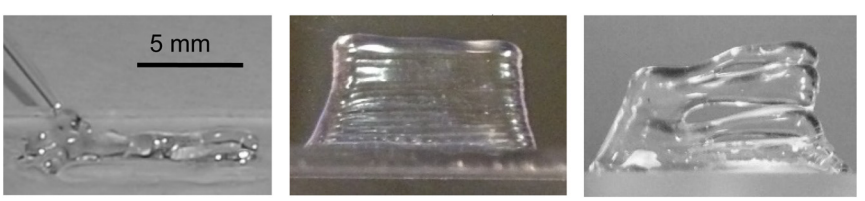

Fig. 4 Morphology of single track wide wall created with different layer-to-layer steps: (a) too small of a layer height, (b) correct layer height, and (c) too great of a layer height.

Downloaded From: https://www.spiedigitallibrary.org/journals/Optical-Engineering on 12/17/2018
Terms of Use: https://www.spiedigitallibrary.org/terms-of-use

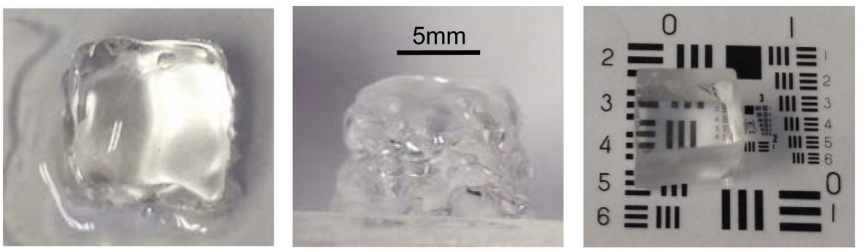

Fig. 5 Printed 3-D cube: (a) top view, (b) side view, and (c) oblique view of sample placed on to a 1951 USAF resolution chart after polishing.

parameters that were used for printing walls ($f = 1$ mm/s, $v = 0.5$ mm/s, $P = 30$ W). The cube was built up with a series of monolayers, and each monolayer was printed with a pattern of single tracks. The space between the tracks was set to be 0.4 mm on each layer. Figures 5(a) and 5(b) show the cube as printed. The undulations from individual layers are visible, but the top layer is very smooth. There are also no noticeable voids in the solid quartz piece. Figure 5(c) shows the cube after polishing with a 1-μm fabric plate. Patterns directly behind the quartz on a 1951 USAF resolution chart may be seen clearly without any obvious distortion. There were no obvious voids in the sample, and it was striae free. This is significant, because it indicates that the tracks are fused together sufficiently to remove the interfaces between the filaments.

3.4 *Printing Curved Surfaces*

A cylindrical lens was printed to demonstrate rudimentary figuring of the surface without polishing. The cylindrical geometry was selected because the 2-D profile is easier to adjust the surface topology. Fused quartz was deposited with a scan speed, feed rate, and laser power of $v = 0.5$ mm/s, $f = 1$ mm/s, and $P = 30$ W, respectively. Three layers were deposited with different number of tracks in the lateral direction depending on the desired radii of curvature for the final geometry. The profiles in Fig. 6 were created using 11, 8, and 3 adjacent tracks for the first, second, and third layers, respectively. A cross section of a deposited sample is shown in Fig. 6(a). After deposition, the surface is reflowed by slowly scanning the laser beam over it using $P = 25$ W and $v = 0.3$ mm/s scan speed. This heats the glass locally and allows surface tension to drive viscous flow.[17] The filament is retracted during this step. Figure 6(b) shows the cross section of the geometry. There is some deviation from the desired cylindrical surface at the interface of the substrate, with some of the asymmetry introduced by feeding the filament from the side (perpendicular to the scanning direction, as shown in Fig. 1). The radius of this cylinder is $R = 4.3$ mm without any other postpolishing.

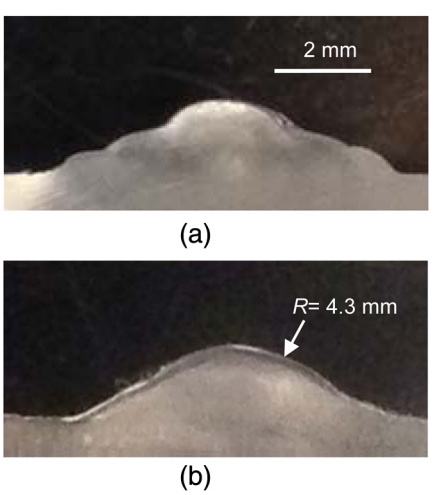

Fig. 6 Cross section of solid cylindrical geometry deposited with laser-heated filament process (a) as printed and (b) after laser-heated reflow.

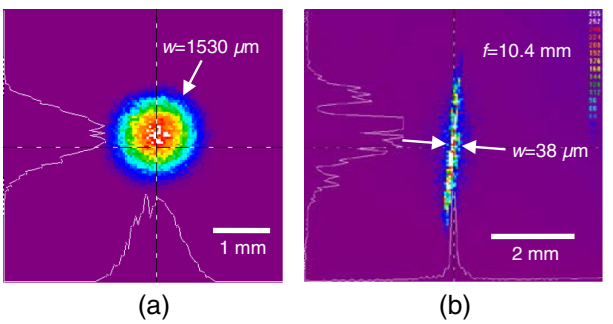

Fig. 7 (a) Profile of the incident laser beam and (b) after focusing 10.4 mm from the planar surface of printed planoconvex printed lens.

The back surface of the substrate is flat and the structure functions as cylindrical planoconvex lens. Figure 7 shows the profile of a $\lambda = 1070$ nm fiber laser (SDL FL10) beam focused by the geometry in Fig. 6. The initial beam has a Gaussian profile with a waist of 1.53 mm. The minimum focused waist is 38 μm at 10.4 mm from the back surface of the lens (~9× the diffraction limit).

3.5 *Optical Measurements*

The transmittance of a 5-mW HeNe laser beam ($\lambda = 632.8$ nm) through a sample of deposited quartz was measured at normal incidence after polishing on both sides. For the 6-mm-thick sample printed with $f = 1$ mm/s, $v = 0.5$ mm/s, and $P = 30$ W, the transmittance was measured to be 0.924. In addition, spectroscopic ellipsometery (M-VASE, J.A. Woollam) was used to measure the index of refraction of the printed fused quartz. At $\lambda = 633$ nm, the index of quartz is $n = 1.468$, corresponding to a reflectance at normal incidence of $R = 0.036$. After accounting for reflectance at both the front and back surfaces, this predicts

Downloaded From: https://www.spiedigitallibrary.org/journals/Optical-Engineering on 12/17/2018
Terms of Use: https://www.spiedigitallibrary.org/terms-of-use

transmittance at normal incidence of 0.929 assuming no losses. This measurement indicates that less than 0.005 of the energy is absorbed or scattered by the printed quartz (an extinction coefficient of $\alpha = 13.2\ \mathrm{m}^{-1}$). This relatively large extinction coefficient is attributed to light scattering within the printed quartz due to small inclusions, including the condensation of vaporized silica soot within the specimen.

An important factor for printed optics is the refractive index homogeneity. Even small index variances inside of the glass will significantly degrade the spatial resolution of an optical system. Figure 8 shows an image of a 1951 USAF test pattern taken through the quartz sample with ambient lighting. The printed quartz window is positioned 10 mm away from the pattern so the light from points in the object space passes through the entire sample before being focused onto the image plane. Qualitatively, this image is similar to an image taken with the same system without the printed quartz window (Fig. 8). One way to quantify the effect of imaging the pattern through the quartz window is to measure the MTF defined as $M = (I_{\max} - I_{\min})/(I_{\max} + I_{\min})$,[22] where $I_{\max}$ is the maximum intensity and $I_{\min}$ is the minimum intensity of fringes on the recorded image. Both images, with and without the sample, are processed in MATLAB® in gray scale. Figure 8(d) compares the MTF for the system with the printed quartz window with that of the system without the window. The MTF of both images starts to drop at 57 mm^{-1} and matches each other very closely, suggesting that any index homogeneity does not limit an $f/\# = 8$ optical system.

3.6 *Mass and Energy Analysis*

Figure 9 shows a thermal simple model of the AM process. The fused quartz filament enters the molten region and exits as a printed track. A mass balance for this model can be expressed as

$$\dot{m}_{\mathrm{in}} - \dot{m}_{\mathrm{out}} = \dot{m}_v, \tag{1}$$

where

$$\dot{m}_{\mathrm{in}} = \rho f(\pi D_f^2/4) \quad \text{and} \quad \dot{m}_{\mathrm{out}} = \rho A_c v. \tag{2}$$

In these expressions, $\dot{m}_v$ is the mass of vaporized fused quartz, ρ is the density of the fused quartz, D_f is the diameter

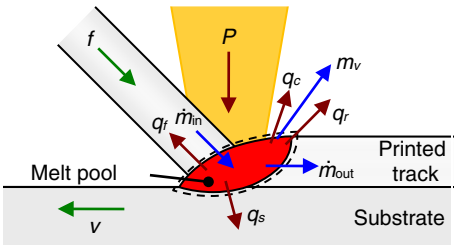

Fig. 9 Mass and energy balance of the molten region.

of the filament, and A_c is the cross-sectional area of the printed track. Solving for the cross-sectional area gives

$$A_c = \frac{\pi}{4}\frac{fD_f^2}{v} - \frac{\dot{m}_v}{\rho v}. \tag{3}$$

The measured cross-sectional area was plotted for different powers in Fig. 3. Equation (3) allows for a calculation of the vaporized mass. The amount of vaporized material scales with the power is significantly higher for lower feed rates.

The energy balance is simplified by modeling the problem as quasisteady state. This assumes that the temperature of the molten region is invariant with the scanning position and is located in the center of a long track or thin wall. Under these conditions, the change in the thermal energy over a control volume surrounding the molten region is zero

$$\Delta E = P - (q_c + q_r + q_f + \dot{m}_v h_v + q_s) = 0, \tag{4}$$

where P is the laser power, h_v is the energy required for vaporizing a unit mass of glass (specific latent heat), q_s is the heat conducted to the substrate, q_f is the heat transfer to the filament, q_r is the net heat transfer exchanged with the surroundings via radiation, and q_c represents the heat lost to the air by convection.

Even at a quasisteady state, the heat transfer from the molten region is a complex process with temperature-dependent thermal properties. The following assumptions are made to significantly simplify the heat transfer analysis: (1) the temperature in the molten region is uniform; (2) the shape of the melt does not change with time; (3) the convection coefficient is taken to be 10 $\mathrm{W/m^2 \cdot K}$, and is temperature independent; and (4) the filament acts as a one-dimensional (1-D) extended surface subject to convection and radiation.

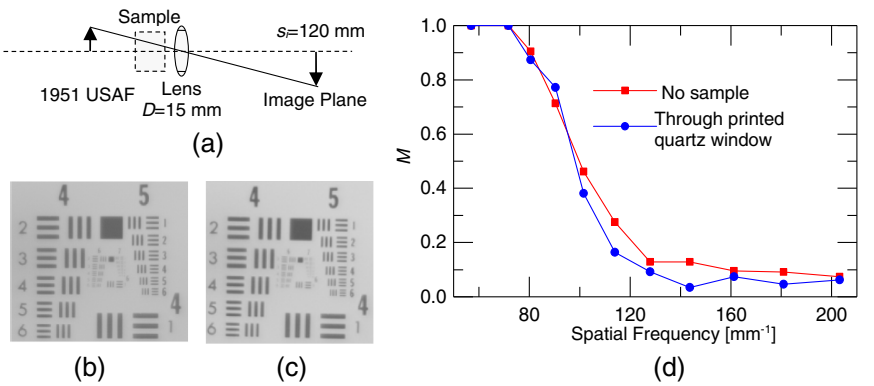

Fig. 8 (a) Imaging setup, (b) image or pattern taken through 6 mm of printed quartz, (c) image of pattern without quartz, and (d) the MTF results for these two images.

Downloaded From: https://www.spiedigitallibrary.org/journals/Optical-Engineering on 12/17/2018
Terms of Use: https://www.spiedigitallibrary.org/terms-of-use

For a hemispherical molten region, the heat lost to the surroundings via convection and radiation is, respectively,

$$q_c = h\left(\frac{\pi}{4}D_m^2\right)(T_m - T_\infty), \tag{5}$$

and

$$q_r = \varepsilon\sigma\left(\frac{\pi}{4}D_m^2\right)(T_m^4 - T_\infty^4), \tag{6}$$

where D_m is the diameter of the molten region, h is the heat convection coefficient, T_∞ is the ambient temperature, ε is the emittance of the glass, and σ is the Stefan–Boltzmann constant.

While some thermal energy is lost due to conduction along the filament, q_f, the amount is not as significant as that with metal wire-fed AM processes. Because the filament is relatively slender, it can be modeled as a 1-D conduction problem with the temperature only varying along the length of the filament (i.e., feeding direction). This temperature distribution may be derived from applying the conservation of energy inside the filament. Combining axial conduction, radiation, and convection, along with advection gives

$$-\frac{d}{ds}\left(k\frac{dT_f}{ds}\right)\left(\frac{\pi D_f^2}{4}\right) - h\pi D_f(T_f - T_\infty) - \varepsilon\sigma\pi D_f(T_f^4 - T_\infty^4) - f\rho A_c c_p\frac{dT_f}{ds} = 0, \tag{7}$$

where T_f is the temperature of the filament at a distance s from the molten region. The boundary conditions for Eq. (7) are as follows: the temperature of the filament where it contacts the molten region is T_m ($T_f|_{s=0} = T_m$), and the filament is long enough that its temperature approaches the surrounding ambient temperature far away from the molten region ($T_f|_{s=\infty} = T_\infty$). T_f along the filament is obtained by solving Eq. (6) with the finite difference method. The heat transfer to the filament, q_f, can then be calculated using Fourier's law

$$q_f = -k\left.\frac{dT}{ds}\right|_{s=0}. \tag{8}$$

SiO_2 gas is not thermodynamically stable at atmospheric pressure and all of the vaporized quartz is converted to SiO by the chemical reaction: $2SiO_2 \Leftrightarrow 2SiO + O_2$.[23] Yang et al. reported that the evaporation of quartz starts to be significant at 2800 K, and is constant with respect to temperature after the temperature surpasses the boiling point (~3100 K).[24] Elhadj et al. reported that the vaporization rate of fused quartz is as follows:[25]

$$V_m'' = \left(6.25\times10^3\frac{\mu g}{\mu m^2\cdot s}\right)\exp\left[\left(-120.1\frac{kcal}{mol}\right)/(RT)\right], \tag{9}$$

where R is the ideal gas constant. This mass flux is applied over the area of the molten region $\dot{m}_v = (\pi D_m^2/4)V_m''$.

The heat conduction from the molten region to the substrate (q_s) is calculated using the finite volume method in ANSYS Fluent. Again, the scanning path is assumed to be infinitely long to discard edge effects. This requires scanning the laser to a point where the peak temperature is invariant with respect to the scanned distance (typically 40 to 60 mm for $v = 0.25$ to 1.0 mm/s). Simulations are run for a full range of laser powers and translation velocities to generate a semiempirical relationship between the temperature of the molten region and the power supplied by the laser. These results are combined with Eqs. (4)–(8) to solve the temperature of the molten region. The results of this simulation are plotted in Fig. 10 for a constant feed rate/scan speed ratio, $f/v = 2$. These results indicate that the temperature of the molten region increases with increasing laser power until such a point that the molten region temperature reaches the vaporization region. The onset of vaporization significantly reduces the rise in temperature with further increasing laser power. As the molten region temperature approaches the boiling point, the energy removed from the system via latent heat dominates the thermal response.

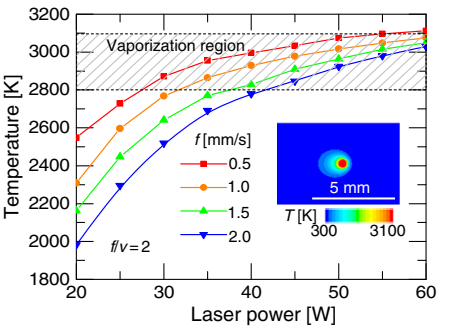

Fig. 10 Molten region temperatures predicted by the energy balance analysis with inset showing surface temperature from fluent model.

The higher molten region temperatures associated with lower feed rates also correspond to lower cross-sectional areas. When the feed rate is $f = 2.0$, the temperature enters the vaporization region for laser powers greater than 40 W. This agrees well with the significant rise in thermal emission observed in the spectroscopic study, including the observation that the peak emission wavelength does not continue to shift with increased laser power for powers greater than 40 W.

In order to validate the thermal modeling results, a LumaSense Impac 140 pyrometer was used to measure the molten region temperature at lower laser powers, as the maximum value of the temperature range for the pyrometer is 2500°C. Figure 11 shows the temperatures measured

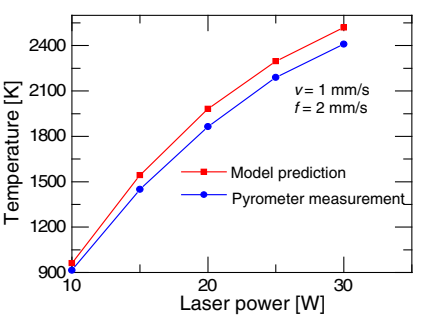

Fig. 11 Molten region temperatures from thermal modeling predictions and pyrometer measurements for $f = 2$ mm/s and $v = 1$ mm/s.

Downloaded From: https://www.spiedigitallibrary.org/journals/Optical-Engineering on 12/17/2018
Terms of Use: https://www.spiedigitallibrary.org/terms-of-use

with the pyrometer compared with the model's predictions. The theoretical temperatures obtained from this model match very closely with experimentally measured values. This finding also agrees the model's prediction that strong vaporization occurs at ~2600°C.

3.7 *Molten Region Radiation Spectra Measurements*

As shown in Fig. 1(b) and predicted by the thermal model, the laser heats the fused quartz to the point that the quartz emits visible light. The intensity of the emitted light varies with the laser power and other process parameters. The emitted light is potentially a useful measurement for feedback control because it relates to the temperature of the molten region. Previous results from laser processing borosilicate glasses[26] showed narrow emission as species in the glass were thermally excited. The lack of significant line emission agrees with the absence of these additives in fused quartz. Figure 12 shows spectral data collected using a spectrometer when depositing single tracks using $f = 2$ and $v = 1$ and with laser powers ranging from 40 to 60 W. All of the data are collected while the laser beam is near the center of the deposition track and after the point where the process becomes steady with respect to scan distance.

Planck's law cannot be used to directly calculate the average temperature of the interrogation region because the interrogation region is not at a uniform temperature. In addition, the molten quartz does not appear to exhibit a gray body spectral response. Despite this, the results show that both the intensity and peak wavelength are correlated with the laser power. The maximum blueshifting occurs between laser powers of 20 and 40 W [Fig. 12(a)]. Above 40 W, the wavelength distribution is constant and only increases in intensity. This transition appears to correspond to the onset of significant vaporization from the molten region.

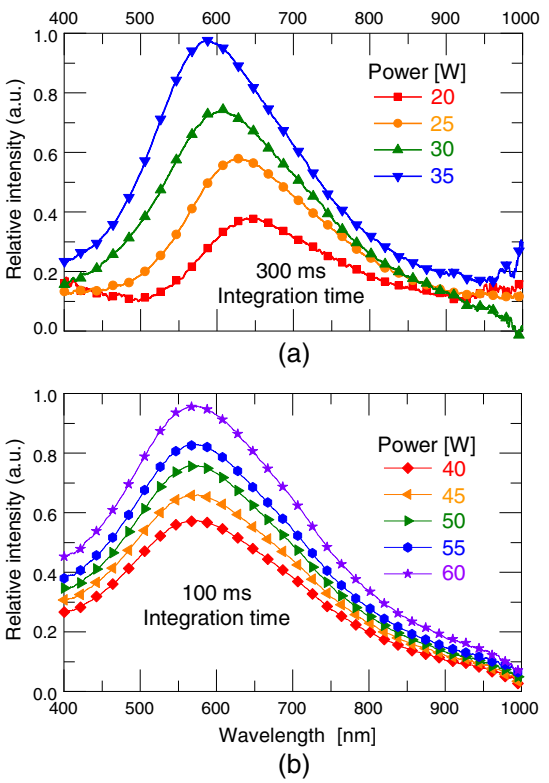

Fig. 12 Emission spectra of fused quartz molten regions with different laser powers (a) $P = 20$ to 35 W measured with 300-ms integration time and (b) $P = 40$ to 60 W measured with 100 ms integration time.

4 Summary and Conclusions

This paper demonstrated AM of transparent GE 214 fused quartz using a filament-fed laser-heated process. Continuous 1-D, 2-D, and 3-D geometries were all successfully deposited. Cylindrical planoconvex geometries with smooth surfaces were also printed to demonstrate control of the surface topology and the potential for refractive optics. Vaporization has a strong effect on the morphology of printed single tracks at higher laser powers and lower feed rates, and spectroscopy shows significantly greater incandescent emission associated with the onset of vaporization. Analysis of mass and energy balances was used to predict the thermal response, and these models substantiate the evaporation and agree with the empirically established operational process window. The modeling result agrees with pyrometer measurements for temperatures lower than 2500°C. Preliminary, optical measurements show that the printed fused quartz cube has a high transmittance and index homogeneity. The coefficient of thermal expansion of fused quartz proves to be advantageous for AM, which may be used to create complex geometries for both optical and structural applications.

Acknowledgments

This work was supported by Missouri S&T Materials Research Center, National Science Foundation (CMMI-1538464), and the Air Force Research Laboratory. The authors are grateful to Ophir for the donation of the NanoScan 2.

References

1. I. Gibson, D. W. Rosen, and B. Stucker, *Additive Manufacturing Technologies*, Springer, New York, New York (2010).
2. E. Brockmeyer, I. Poupyrev, and S. Hudson, "PAPILLON: designing curved display surfaces with printed optics," in *Proc. of the 26th Annual ACM Symp. on User Interface Software and Technology*, pp. 457–462, ACM, St. Andrews, Scotland (2013).
3. K. D. D. Willis et al., "Printed optics: 3D printing of embedded optical elements for interactive devices," in *Proc. of the 25th Annual ACM Symp. on User Interface Software and Technology*, pp. 589–598, ACM, Cambridge, Massachusetts (2012).
4. T. Pereira, S. Rusinkiewicz, and W. Matusik, "Computational light routing: 3D printed optical fibers for sensing and display," *ACM Trans. Graph.* **33**(3), 1–13 (2014).
5. K. Blessing and R. van de Vrie, "Print head, upgrade kit for a conventional inkjet printer, inkjet printer and method for printing optical structures," US Patent 8840235B2, Luxexcel Holding Bv., United States (2014).
6. A. C. Urness et al., "Liquid deposition photolithography for submicrometer resolution three-dimensional index structuring with large throughput," *Light: Sci. Appl.* **2**(3), e56 (2013).
7. T. Niino and H. Yamada, "Fabrication of transparent parts by laser sintering process: transparentization of laser sintered plastic parts by infiltrating thermosetting epoxy with tuned refractive index," *J. Jpn. Soc. Precis. Eng.* **75**(12), 1454–1458 (2009).
8. S. R. Marder, J.-L. Brédas, and J. W. Perry, "Materials for multiphoton 3D microfabrication," *MRS Bull.* **32**(07), 561–565 (2007).
9. M. J. Weber, *Handbook of Optical Materials*, CRC Press, Boca Raton, Florida (2002).
10. F. Klocke, A. McClung, and C. Ader, "Direct laser sintering of borosilicate glass," in *Proc. of the 15th Annual SFF Symp.*, pp. 214–219, University of Texas, Austin, Texas (2004).
11. M. Fateri and A. Gebhardt, "Selective laser melting of soda-lime glass powder," *Int. J. Appl. Ceram. Technol.* **12**(1), 53–61 (2015).
12. Q. Fu, E. Saiz, and A. P. Tomsia, "Bioinspired strong and highly porous glass scaffolds," *Adv. Funct. Mater.* **21**(6), 1058–1063 (2011).

Downloaded From: https://www.spiedigitallibrary.org/journals/Optical-Engineering on 12/17/2018
Terms of Use: https://www.spiedigitallibrary.org/terms-of-use

13. G. Marchelli et al., "The guide to glass 3D printing: developments, methods, diagnostics and results," *Rapid Prototyp. J.* **17**(3), 187–194 (2011).
14. R. S. Khmyrov et al., "Crack-free selective laser melting of silica glass: single beads and monolayers on the substrate of the same material," *Int. J. Adv. Manuf. Technol.* **85**, 1461–1469 (2016).
15. D. T. Nguyen et al., "3D-printed transparent glass," *Adv. Mater.* **29**, 1701181 (2017).
16. F. Kotz et al., "Three-dimensional printing of transparent fused silica glass," *Nature* **544**, 337–339 (2017).
17. V. P. Veiko, A. K. Kromin, and E. B. Yakovlev, "Laser technologies for micro-optics fabrication," *Proc. SPIE* **1874**, 93–102 (1993).
18. V. P. Veiko and K. K. Kieu, "Laser amorphisation of glass ceramics: basic properties and new possibilities for manufacturing microoptical elements," *Quantum Electron.* **37**, 92–98 (2007).
19. J. Luo et al. "Additive manufacturing of transparent soda-lime glass using a filament-fed process," *J. Manuf. Sci. Eng.* **139**(6), 061006 (2017).
20. J. Klein et al., "Additive manufacturing of optically transparent glass," *3D Print. Addit. Manuf.* **2**(3), 92–105 (2015).
21. R. Kitamura, L. Pilon, and M. Jonasz, "Optical constants of silica glass from extreme ultraviolet to far infrared at near room temperature," *Appl. Opt.* **46**(33), 8118–8133 (2007).
22. G. D. Boreman, *Modulation Transfer Function in Optical and Electro-Optical Systems*, SPIE Press Bellingham, Washington (2001).
23. D. B. Chang, J. E. Drummond, and R. B. Hall, "High-power laser radiation interaction with quartz," *J. Appl. Phys.* **41**(12), 4851–4855 (1970).
24. S. T. Yang et al., "Thermal transport in CO_2 laser irradiated fused silica: In situ measurements and analysis," *J. Appl. Phys.* **106**(10), 103106 (2009).
25. S. Elhadj et al., "Heating dynamics of CO_2-laser irradiated silica particles with evaporative shrinking: Measurements and modeling," *J. Appl. Phys.* **111**(9), 093113 (2012).
26. J. Luo et al., "Bubble formation in additive manufacturing of glass," *Proc. SPIE* **9822**, 98220D (2016).

Junjie Luo received his MS degree in thermal engineering from Guangzhou Institute of Energy Conversion in 2011 and his PhD in mechanical engineering from Missouri University of Science and Technology in 2017. His research interests include additive manufacturing, thermal science, optical-mechanical design, and CFD simulation.

John M. Hostetler is a master's student in mechanical engineering at Missouri University of Science and Technology. His research focuses on the additive manufacturing of optical glass, particularly free-standing low-CTE structures using optical fibers as a feed stock. In addition, he has also studied the diffusion of optical property modifiers in localized laser-heated melts and the selective laser sintering of low-density/CTE glass parts.

Jonathan T. Goldstein received his PhD in physics from the University of Illinois at Urbana Champaign in 1996 and has been working since then at the Air Force Research Lab Materials and Manufacturing Directorate, in Dayton, Ohio. During the last several years, he has focused on a variety of bulk glasses as well as laser treatments of glasses and ceramics, including laser sintering of ceramic YAG fiber, selective laser sintering of silica powders, and glass fiber processing for fiber-fed laser-fused deposition.

Douglas A. Bristow received his BS degree in mechanical engineering from Missouri S&T in 2001 and his MS and PhD degrees, also in mechanical engineering, from the University of Illinois at Urbana-Champaign in 2003 and 2007, respectively. He joined Missouri S&T in 2008, where he is currently an associate professor in the Department of Mechanical and Aerospace Engineering and the director of the Center for Aerospace Manufacturing Technologies. His research interests include repetitive and iterative learning control, atomic force microscopy, additive manufacturing process control, and volumetric error compensation in machine tools and robotics.

Robert G. Landers received his PhD in mechanical engineering from the University of Michigan in 1997 and has been a professor at Missouri S&T since 1999. His research and teaching interests are in the areas of modeling, analysis, monitoring, and control of manufacturing processes, estimation and control of electrochemical alternative energy systems and electrohydraulic systems, and digital control applications.

Edward C. Kinzel received his MS and PhD degrees in mechanical engineering from Purdue University in 2003, 2005, and 2010, respectively, focusing on laser-based micro/nanofabrication including laser forward transfer and selective laser sintering of electronics as well as near-field direct-write nanolithography with sub-100 nm resolution. He has been an assistant professor at Missouri S&T since 2012, where his research as focused on the scalable manufacturing of IR-FSS/metasurfaces and thermal transport problems in additive manufacturing, including glass printing.

Biographies for the other authors are not available.

Downloaded From: https://www.spiedigitallibrary.org/journals/Optical-Engineering on 12/17/2018
Terms of Use: https://www.spiedigitallibrary.org/terms-of-use